Investigation and Modeling of DC Bias Impact on Core Losses at High Frequency

Bima Nugraha Sanusi, *Graduate Student Member, IEEE*, Mathias Zambach, Cathrine Frandsen, Marco Beleggia, Anders Michael Jørgensen, and Ziwei Ouyang, *Senior Member, IEEE*

***Abstract*—This article aims to study the core losses behavior at high frequency (MHz range) with superimposed dc bias in ferrite. Inductive compensation method is employed in the measurement circuit to reduce sensitivity to phase errors. An addition to the circuit is proposed in this work to make easier dc bias generation. Furthermore, a detailed measurement accuracy consideration is also discussed. The tested MnZn ferrite has a nominal relative permeability of 1500 and 800, which was tested at frequency from 500 kHz to 3 MHz. The measurement results are explained thoroughly with three controlling parameters: excitation frequency, peak ac flux density, and dc bias. There are several important findings. First, a higher dc bias creates higher losses at the same frequency and ac flux density. Second, at the same dc bias and ac flux density, higher frequency generates a lower relative losses increase. This second point has not been seen in the previous literature and is elaborated more in Section III-B. Third, the measurement result shows how dc bias increases the hysteresis loop area and coercivity. The first and third findings confirm the existing literature findings. As a final step, an improved Steinmetz Premagnetization Graph and artificial neural network are used to create core loss prediction model. The measurement data and the built model can be accessed online for use by other magnetics designer.**

***Index Terms*—Core losses, core losses measurement, core losses modeling, dc bias, high frequency.**

I. Introduction

IT IS increasingly necessary to know core losses with reasonable accuracy in the intended application. This is to avoid overheating on the one hand and oversizing on the other. There are two steps in understanding the core losses. The first is measuring the core losses to know the behavior of the core. The second is modeling the core losses to predict what losses are going to occur under a certain condition. The designer may skip the first step by relying on the published core losses data from the manufacturer. However, the intended application may have different core geometry, excitation waveform, and operating condition than the published data. This will have an impact on the core losses prediction accuracy. The modeling stage aims to predict the core losses based on a set of measurement data. With accurate measurement and modeling, the designer can find the optimal point in the magnetic component design.

Magnetism is an inherently quantum mechanical property of matter [1]. It makes the core losses mechanism in magnetic material very complex. Design engineers normally acknowledge two main sources of core losses: hysteresis loss and eddy current loss [2], [3]. One can calculate hysteresis losses by minimizing the magnetic energy of a system with magnetocrystalline anisotropy under the influence of an applied field [1]. However, the manufacturing process alters the shape and microscopic structure of a magnetic core [4], thereby influencing the hysteresis behavior and complicating the problem significantly. Eddy current loss can be seen at two levels. First, at the bulk level, eddy currents will form to counter the magnetic flux through the core cross section. Second, at the grain level, the nonuniform magnetization creates eddy current around the domain walls. The grain-level phenomenon is also called excess eddy current losses [5], [6].

There are numerous ways to model the magnetic core losses. They can be classified as the following.

1) *Hysteresis Loop Based:* The dissipated energy per cycle is determined from the hysteresis loop area. The Preisach [7], [8] and Jiles-Atherton models are examples of this. The approach is accurate but requires many parameters and accurate hysteresis loop measurement.
2) *Steinmetz Equation (SE) [9] Based:* Core losses per volume is modeled by the power equation. From there stems various models [10], [11], [12], [13], [14], which attempt to improve the loss prediction accuracy under different excitation.
3) *Loss Map Based:* Core losses are obtained by interpolation of measurement results data. The loss map can accommodate different flux density, frequency, etc. The examples are given in [15], [16]. The approach is practical but relies heavily on measurement data.
4) *Loss Separation Based:* The total power losses are constructed by calculating separately the hysteresis loss and

Manuscript received 7 October 2022; revised 5 January 2023; accepted 10 February 2023. Date of publication 24 February 2023; date of current version 20 April 2023. This work was supported by Danmarks Frie Forskningsfond Project under Grant 9041-00231B. An earlier version of this article was presented at the Applied Power Electronics Conference 2022 and European Conference on Power Electronics and Applications 2022 Conference. Recommended for publication by Associate Editor M. Chen. *(Corresponding author: Ziwei Ouyang.)*

Bima Nugraha Sanusi and Ziwei Ouyang are with the DTU Electro, Danmarks Tekniske Universitet, 2800 Kgs. Lyngby, Denmark (e-mail: bnusa@elektro.dtu.dk; zo@elektro.dtu.dk).

Mathias Zambach and Cathrine Frandsen are with the DTU Physics, Danmarks Tekniske Universitet, 2800 Lyngby, Hovedstaden, Denmark (e-mail: zambach@fysik.dtu.dk; fraca@fysik.dtu.dk).

Marco Beleggia and Anders Michael Jørgensen are with the DTU Nanolab, Danmarks Tekniske Universitet, 2800 Lyngby, Hovedstaden, Denmark (e-mail: mabele@dtu.dk; ajoe@dtu.dk).

The online dataset is available on https://dx.doi.org/10.21227/7khj-bd03.

Color versions of one or more figures in this article are available at https://doi.org/10.1109/TPEL.2023.3249106.

Digital Object Identifier 10.1109/TPEL.2023.3249106

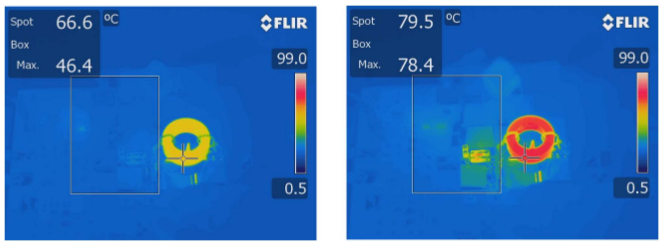

Fig. 1. Magnetic core temperature comparison: without DC bias (left) and with DC bias (right). The spot temperature is capturing the core temperature, while the box temperature is showing the current sense resistor temperature.

eddy current loss and summing them. The calculation uses basic core geometry and material properties, such as conductivity and coercivity. This approach was demonstrated in [3] and [17]. It is useful when extensive measurement data are not available.

The SE-based model is the most adopted approach by magnetics designer. This is due to the practicality of power formulas. However, measurement data are necessary for this approach.

Core loss measurement techniques can be classified into calorimetric and electric method. Calorimetric method works are based on the energy conservation law. The core losses create heat. The heat is measured in the form of temperature rise. From temperature rise and thermal properties, the core losses can be estimated. This method is well known. A recent work [18] uses the transient principle to reduce measurement time. The major drawback of this method is the difficulty to separate winding loss. The electric method can avoid this drawback. It works by measuring the induced voltage and excitation current. The induced voltage measurement automatically excludes the winding losses. Therefore, this method is chosen in this article.

Methods such as [12], [13], [19] can be used to predict core losses with any excitation waveform. However, their validity needs to be reinvestigated. Those models work under the assumption of nonchanging Steinmetz parameters. Unfortunately, the Steinmetz parameters can change at higher frequency [20], [21] or in the presence of dc bias [22], [23], [24]. Fig. 1 shows the change in magnetic core temperature when dc bias flux is applied. There is also a missing experimental verification for core losses under square wave excitation at higher frequency. Recent reports in [18] and [25] measure losses only under sine wave excitation. The authors in [26], [27], [28], and [29] measure losses with square wave excitation only up to 500 kHz. Therefore, this article aims to provide more insight to core losses by providing comprehensive measurement results and analysis in the frequency range and magnetic materials, which have not been presented before.

The focus of this work is to investigate magnetic core losses under square wave excitation with dc bias. The frequency of interest is up to 3 MHz. The dc bias impact will be quantified and the current core losses model will be extended or modified to incorporate the impact. Behavior in different core material is also investigated. Through the end, we will see if the current losses model still matches experimental measurement. The parameter shift, if there is any, will also be analyzed.

II. Core Losses Measurement Setup

A. Measurement Principle

The main difficulty in measuring core losses with electric method is that ferrites generally have low losses compared to the stored energy. This creates the phase angle ϕ between v_{DUT} and i (indicated in Fig. 2) close to 90°, since the impedance of magnetizing inductor $L_{\mathrm{m,DUT}}$ is much smaller than the equivalent core loss resistance $R_{\mathrm{Fe,DUT}}$. The relative power error caused by the phase discrepancy $\Delta\phi$ for sinusoidal excitation is given by (1), which was derived in [30]. It is virtually impossible to eliminate $\Delta\phi$ in an actual measurement setup. Therefore, a more effective solution to limit the power error is to control $\tan(\phi)$

$$\left|\frac{\Delta P}{P}\right| = |\tan(\phi)| \cdot |\Delta\phi| \,. \tag{1}$$

The mutual inductance neutralization [31] or inductive cancellation [26] technique can bring $\tan(\phi)$ to a more feasible region. However, this method requires a very accurate compensating inductance or capacitance. This is not easy to design. A more recent improvement of this cancellation concept [27] allows a less strict compensation requirement. This is called partial cancellation concept and is done by introducing the cancellation factor k, which will be explained below. The same concept is adopted in this work but with the addition of dc bias injection.

The core losses measurement circuit is shown in Fig. 2. R_{p} and L_{p} represent the winding resistance and stray inductance, respectively, on the primary side. On the secondary side, they are represented by R_{s} and L_{s}. L_{m} is the magnetizing inductance. A dc blocking capacitance C_{DC} is necessary to avoid saturation in the magnetic core. Current sensing is done by measuring voltage across the resistor R_{sense}. However, due to component nonideality, a parasitic inductance L_{sense} will also be present. Parasitic capacitances from measurement devices are shown by C_{diff}.

Although having low winding resistance and stray inductance $(R_{\mathrm{p}}, L_{\mathrm{p}}, R_{\mathrm{s}}, L_{\mathrm{s}})$ is desirable, it should not affect measurement accuracy, since the electrical method will exclude the voltage drop on these elements. High winding resistance and stray inductance on the primary side may limit the circuit operation due to their voltage drop, rendering a higher input voltage requirement to get the desired $\hat{B}$ excitation. On the secondary side, R_{s} and L_{s} will create extra voltage drop if the current flowing is nonnegligible. R_{s} in particular will create the error due to nonzero average power. Therefore, it should be kept as low as possible. More details are given in the following section.

As the focus of this work is core loss under square wave excitation with dc bias, a half bridge circuit is used to generate the excitation. With a symmetric 50% duty cycle in the half bridge, $V_{\mathrm{in}}/2$ will appear at C_{DC}. Then, a controllable dc current source (such as [32]) is placed in parallel to C_{DC} to generate the dc bias. The dc current I_{DC} will flow on top of the ac component, creating H_{DC} excitation in the magnetic core. It is important to use an isolated dc current source here because C_{DC} nodes are floating. In terms of sequence, the dc current is turned ON after the ac excitation has reached steady state,

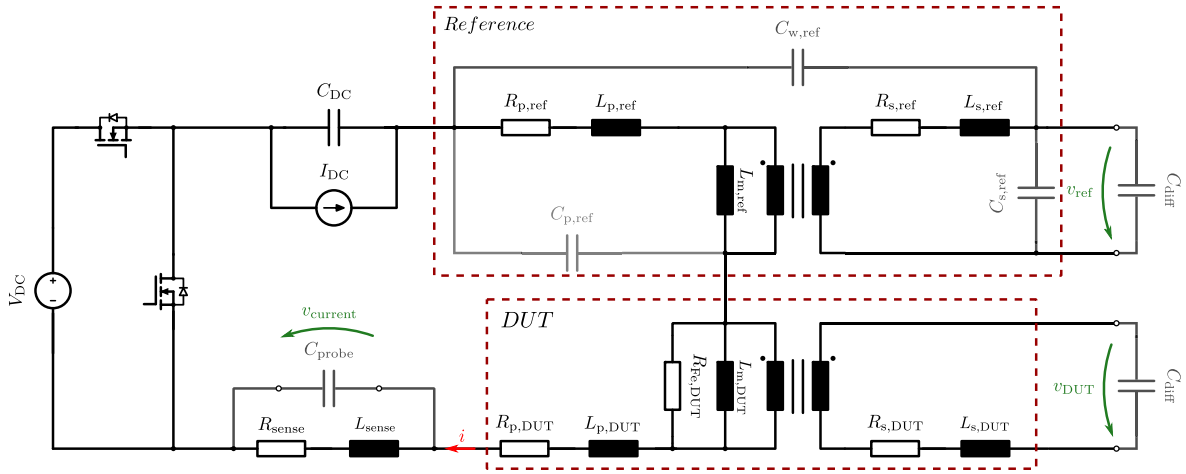

Fig. 2. Electrical circuit of the core losses measurement system. DUT means the magnetic device under test and ref means the reference or compensation element. Magnetic core losses is represented by $R_{\mathrm{Fe,DUT}}$.

in this case 1 ms is the interval between half bridge turn ON and the dc turn ON. Afterward, 100 ms interval is given before any measurement is acquired, to make sure the dc bias and ac excitation have reached steady state. The sequence is repeated for every measured operating point.

In principle, the compensation element (*reference* in Fig. 2) must be chosen to have magnetizing inductance $L_{\mathrm{m,ref}}$ as close as possible to $L_{\mathrm{m,DUT}}$, and much lower core losses compared to the *DUT*. However, when measuring low losses core, it is difficult to find a magnetic core with much negligible core losses, compared to *DUT*. Therefore, we chose to make the reference element by air core inductor which does not have core losses, hence no parallel resistance to $L_{\mathrm{m,ref}}$. A photo of the real life implementation is given in Appendix A. Meanwhile, for the mismatching L_{m}, the cancellation factor in (3) will compensate for it when calculating the loss in (2). Therefore, an exact matching between $L_{\mathrm{m,ref}}$ and $L_{\mathrm{m,DUT}}$ is not necessary.

Based on the measurement circuit, the core losses can be calculated by (2), where T_{sw} is the switching period. For a square wave excitation, the cancellation factor k is calculated by (3), where $V_{\mathrm{ref,pp}}$ is the peak-to-peak value of reference element induced voltage (v_{ref}), and $V_{\mathrm{DUT,pp}}$ is the peak-to-peak value of DUT induced voltage (v_{DUT}). This factor represents the percentage of cancelled reactive voltage to the total reactive voltage. Alternatively, it can be seen that the partial cancellation mechanism creates a virtual voltage $v_{\mathrm{comp}} = v_{\mathrm{DUT}} - v_{\mathrm{ref}}/k$ to replace the initial v_{DUT}. As a result, the phase shift between v_{comp} and measured current (i_{meas}) can be kept minimum, even when the reference element value $L_{\mathrm{m,ref}}$ has a mismatch with $L_{\mathrm{m,DUT}}$. Therefore, the measurement error can be minimized

$$P_{\mathrm{Fe}} = \frac{1}{T_{\mathrm{sw}}}\left(\int_0^{T_{\mathrm{sw}}} v_{\mathrm{DUT}} \cdot i_{\mathrm{meas}}\, dt - \frac{1}{k}\int_0^{T_{\mathrm{sw}}} v_{\mathrm{ref}} \cdot i_{\mathrm{meas}}\, dt\right) \tag{2}$$

$$k = \frac{V_{\mathrm{ref,pp}}}{V_{\mathrm{DUT,pp}}}. \tag{3}$$

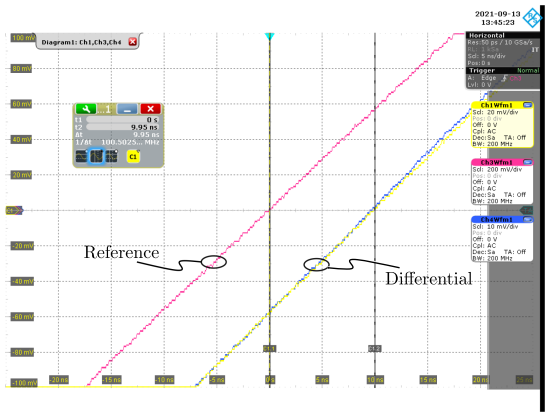

Fig. 3. Voltage measurement comparison: passive probe (reference) and two differential probes. About 10 ns time delay is observed while the gradient is identical.

B. Voltage Measurement

Differential voltage probes are used for the voltage measurement because of the floating measurement position. We chose 25 MHz active differential probe from Testec [33]. An additional benefit of the differential probe is the low parasitic capacitance. In this case, it has an equivalent capacitance of 2.75 pF, which is lower compared to 10 pF of common passive probes. One typical drawback is the measurement delay and rise time. Therefore, the differential probes are calibrated to generate identical waveform as measured by a 200 MHz passive probe, before any measurements are performed. A comparison of the waveforms is shown in Fig. 3. The postprocessing step will compensate the time delay based on the calibration data, hence minimizing the voltage reading error.

Voltage measurements (v_{ref} and v_{DUT}) are influenced by the parasitic capacitances. In the DUT, intra and interwinding capacitances are minimized by using only 1 turn for primary and secondary winding, and keeping enough distance between both windings. This effort is shown in the photos in Appendix A. Therefore, DUT's parasitic capacitances can be neglected in

TABLE I
NOMINAL PARASITIC COMPONENTS VALUE CONSIDERED FOR ERROR CALCULATION

Parameters	Value
$C_{\mathrm{diff,nom}}$	2.75 pF
$C_{\mathrm{w,ref,nom}}$	50 pF
$C_{\mathrm{p,ref,nom}}$,$C_{\mathrm{s,ref,nom}}$	10 pF
$R_{\mathrm{p,ref}}$,$R_{\mathrm{s,ref}}$	200 mΩ
$L_{\mathrm{p,ref}}$,$L_{\mathrm{s,ref}}$	80 nH
$R_{\mathrm{p,DUT}}$,$R_{\mathrm{s,DUT}}$	100 mΩ
$L_{\mathrm{p,DUT}}$,$L_{\mathrm{s,DUT}}$	40 nH
$L_{\mathrm{m,DUT}}$	500 nH
$R_{\mathrm{Fe,DUT}}$	2000 Ω
ω	$2 \cdot \pi \cdot [1...5]$ MHz
k	[0.7...0.8]

this work. The reference air core needs more winding turns and closer distance between primary and secondary. It makes the parasitic capacitances nonnegligible. In particular, $C_{\mathrm{w,ref}}$ and $C_{\mathrm{s,ref}}$ will influence the voltage reading. Those capacitances cause extra current flow, which makes a voltage drop on secondary $R_{\mathrm{s,ref}}$. This voltage drop is included in the voltage measurement and will affect the power calculation.

The work in [27], which introduces the partial cancellation concept, did not provide a clear derivation and calculation of the error caused by those parasitic elements. Therefore, this work also tried to complete the error analysis. The full derivation of measurement error factor ($\Delta P/P$) is presented in Appendix B. To estimate the error, the main and parasitic component values in Fig. 2 need to be defined. Most of them are tied to the hardware, therefore will be constant, except $R_{\mathrm{Fe,DUT}}$, which changes with the operating points, since it represents the core losses. This value can be calculated by (4), where $V_{\mathrm{DUT,rms}}$ is the rms voltage of DUT and P_{Fe} is the calculated core losses. The assumed worst case values of the relevant parameters are listed in Table I. These values will create an overestimation of the error because they combine the worst cases, which may not happen at the same time. For example, $R_{\mathrm{Fe,DUT}} \approx 250\ \Omega$ at 1 MHz 10 mT excitation, and lower at higher frequency, but the same value is used to calculate error at 5 MHz. In Table I the values represent the extreme cases, which may not be touched in this experiment. Nevertheless, it shows the robustness of this method with regards to parasitic capacitances

$$R_{\mathrm{Fe,DUT}} = \frac{V_{\mathrm{DUT,rms}}^2}{P_{\mathrm{Fe}}}. \tag{4}$$

The expected error results are given in Figs. 4, 5, 6 for three different source of parasitic capacitances. When calculating the effect of one capacitance, the others are kept at their nominal value, given in Table I. There is a linear relationship between the capacitance value and the error percentage. It can be seen that the interwinding capacitance $C_{\mathrm{w,ref}}$ brings the highest error to measurement. Nevertheless, the expected total error is still less than 5%.

C. Current Measurement

Current sensing is a critical part of the measurement system. Shunt resistor is chosen over current probe such as [34] mainly due to the dc current measuring capability and bandwidth requirement. The shunt resistor needs to have high precision with low stray inductance. Metal foil chip resistor from Susumu PRL series is used in this work. The shunt resistor has $R_{\mathrm{sense}} = 0.1\ \Omega$ and $L_{\mathrm{sense}} = 1$ nH as the nominal values, which is shown in Fig. 7. In this work's frequency of interest range (500 kHz–3 MHz), the deviation of R_{sense} and L_{sense} from the nominal value is less than 10%. The shunt voltage is measured by the voltage probe, which brings the parasitic capacitance C_{probe}. Its nominal value is 9.5 pF for the RT-ZP10 from Rohde & Schwarz [35], which is used in this work. Passive probe can be used because the negative side is connected to ground. In addition, it provides high enough bandwidth, which is 200 MHz in this case.

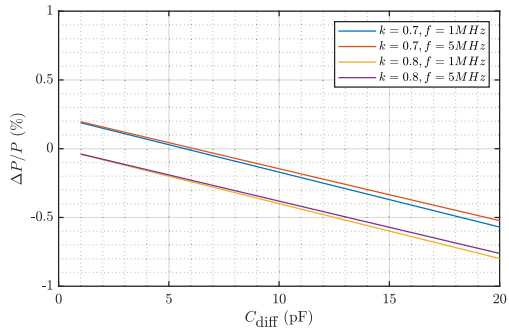

Fig. 4. Error of P_{Fe} measurement as a function of the probe capacitance (C_{diff}).

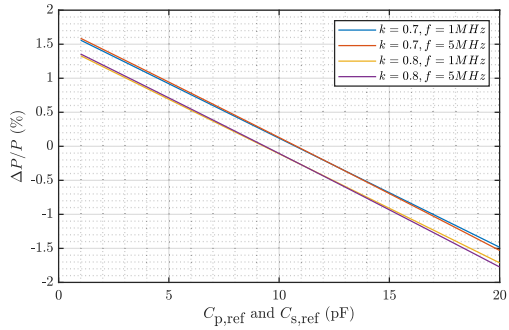

Fig. 5. Error of P_{Fe} measurement as a function of the intra-winding capacitance (C_{p} and C_{s}). Symmetry is assumed between primary and secondary.

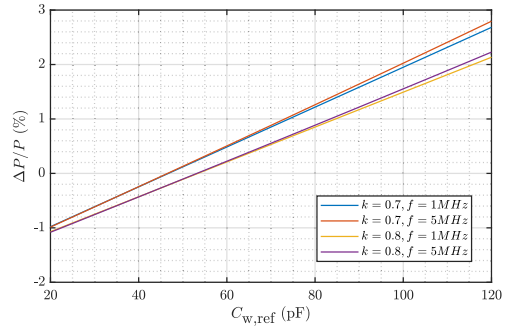

Fig. 6. Error of P_{Fe} measurement as a function of the interwinding capacitance ($C_{\mathrm{w,ref}}$).

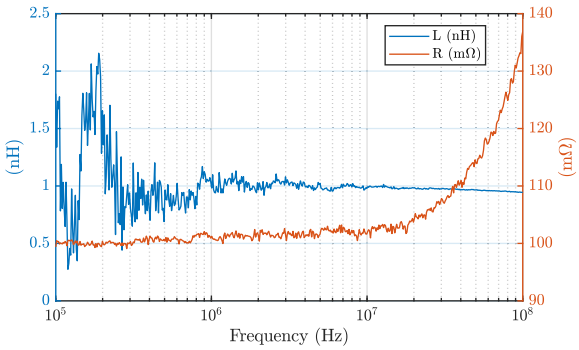

Fig. 7. Current shunt equivalent resistance and inductance.

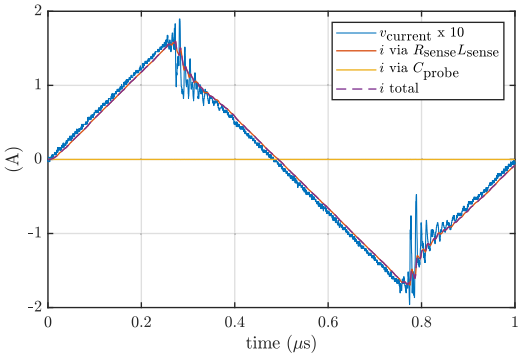

Fig. 8. Current measurement comparison: directly measured voltage and calculated current.

The last step in current measurement is to transform the measured voltage into current. The stray inductance L_{sense} and voltage probe capacitance C_{probe} make the transformation less straightforward. The measured voltage v_{current} needs to be filtered by transfer function as shown in (5). The difference in measured voltage and calculated current is shown in Fig. 8. It can be seen that almost zero current is flowing through C_{probe}. Meanwhile, there is a small phase shift between the voltage measurement (v_{current}) and the *real* current (i_{total}). Hence, this approach anticipates the phase discrepancy brought by the shunt stray inductance, if we use the postprocessed i_{total} in calculating the core losses.

$$i(s) = v_{\text{current}}(s)\left(\frac{1}{s \cdot L_{\text{sense}} + R_{\text{sense}}} + s \cdot C_{\text{probe}}\right). \quad (5)$$

D. Other Accuracy Consideration

Several other sources of error that can affect the measurement are also listed below.

1) *Oscilloscope time resolution limit:* A 0.1 ns resolution means an uncertainty of 0.108° at 3 MHz frequency. Assuming $\tan(\phi) = 1$ and using (1), this translates to power error of 0.19%.
2) *Oscilloscope vertical (ADC) resolution:* An 8 b ADC is used in this work. When capturing the waveform, the vertical scale should be adjusted to make the waveform cover more than 75% of vertical window (10 divisions), hence maximizing ADC resolution usage.

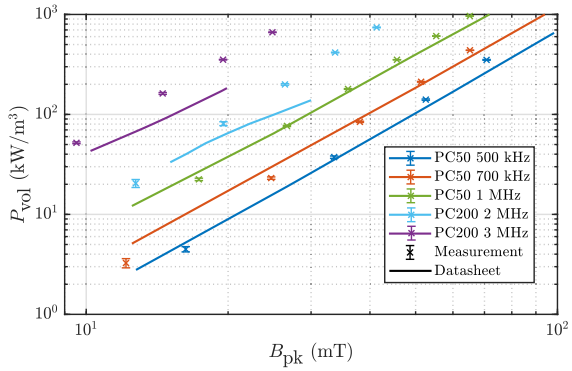

Fig. 9. Comparison between datasheet values and measurement results with sinusoid excitation. Crosses with error bars demonstrate measurement results, and lines demonstrate datasheet values. Different materials and frequency are represented by different colors.

3) Core temperature is assumed to be at room temperature (25 °C–30 °C). This is ensured by short excitation period (100 ms) and enough interval between measurement points, e.g., 10 s. Hence, core losses variation due to changing core temperature is avoided.
4) *Current shunt resistance drift:* The shunt resistor [36] has a temperature coefficient of ± 50 ppm/°C. This means that a 100 °C temperature increase will shift resistance by 5 mΩ, which translates to 0.5% error for $R_{\text{sense}} = 0.1\ \Omega$.

E. Setup Verification

The setup is verified by testing toroid core under sine wave excitation. This is done by replacing the dc source and half-bridge circuit with a power amplifier, which is controlled by a signal generator. Then, the measurement results are compared with datasheet values. The measured cores are PC50 R22.1/13.7/7.9 and PC200 R15.8/8.9/4.7 from TDK. Fig. 9 shows the comparison result. The measurement point is given together with its uncertainty range, which is derived from ten measurement captures.

Measurement results match the datasheet values up to 1 MHz for PC50 material. However, for PC200 material, there is a discrepancy and the measurement gives higher losses than datasheet values. This discrepancy can happen in real practice [37], [38], especially as the frequency goes higher. There can be two reasons for this. First, the material production tolerance, such as the permeability level, can have up to 25% difference which affect the core loss too. The second is how the datasheet values are generated. In the industry, the *B–H* analyzer from [39] is often used to measure core loss to fulfill IEC620444-3 standard. The SY-8219 variant of the machine is generally not very precise for measurement above 1 MHz. Furthermore, this equipment normally does not have compensation element, like in this article, which makes measurement sensitive to phase delay errors. Nevertheless, the analysis of core loss behavior in the next sections will be based on the results from the current setup, not the datasheet value. Hence, having the same zero reference for the analysis. The discrepancy shown here should not change the behavior analysis result.

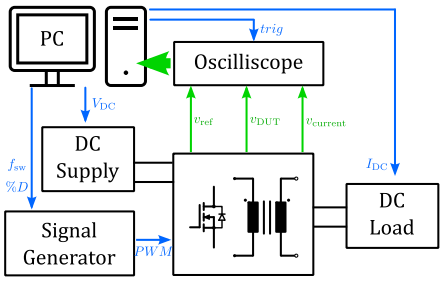

Fig. 10. Architecture of losses measurement system. Blue lines show commands, while green lines show measurement data flow.

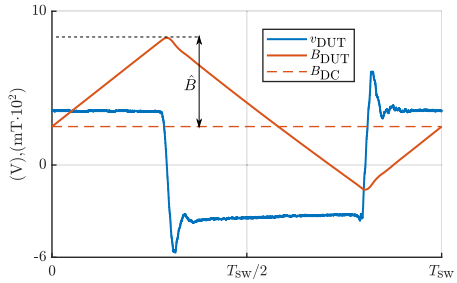

Fig. 11. Sensed DUT voltage (v_{DUT}) and the calculated flux density (B_{DUT}). This example is taken from core sample B at 1 MHz switching frequency.

TABLE II
CORE UNDER TEST

Parameters	Core A	Core B
Core Material	PC50	PC200
Core Geometry	R 22.1/13.7/7.9	ER 14.5/6
V_e	1763 mm^3	334 mm^3
A_e	32.6 mm^2	17.6 mm^2
l_e	54.2 mm	19 mm
Initial μ_r	1500	800
B_{sat} at 25°C	490 mT	480 mT
Intended f_{sw}	0.3–1 MHz	1–3 MHz

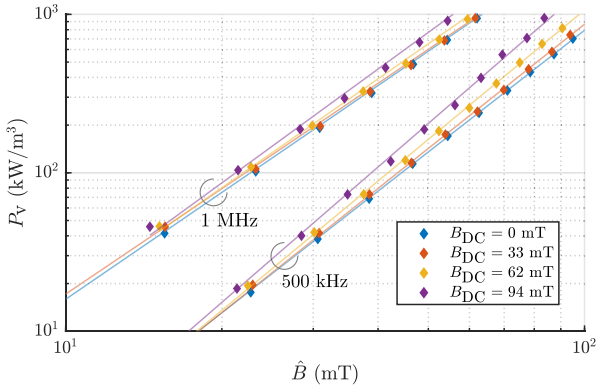

Fig. 12. Core losses density (P_v) versus flux density ($\hat{B}$) measured on test core A with different DC flux bias (B_{DC}) and frequency. 1 mT of B_{DC} translates to 0.53 A/m of H_{DC}.

F. System Architecture

The final step in setting up the measurement system is to make the test automation. The benefit of automation is not only reducing the manual labor, but also ensuring the measurement repeatability. The measurement system architecture is shown in Fig. 10. The circuit block in the middle is detailed previously in Fig. 2. The PC runs a Python program, which controls the measurement sequence. The measured waveforms from oscilloscope are then sent back to the PC to be processed.

III. EXPERIMENTAL INVESTIGATION

This work aims at measuring and analyzing core losses under square wave excitation from frequency of 500 kHz up to 3 MHz. The frequency range is motivated by state-of-the-art commercially available MnZn ferrite for power electronics application [40], [41], [42]. The measurements were performed on two magnetic cores with different relative permeability (μ_r) level. They are listed in Table II along with their detailed properties. V_e, A_e, and l_e mean the magnetic core volume, effective cross section, and mean magnetic path length, respectively. The complete measured inductance values are presented in Appendix A.

The measurement setup was discussed in the previous section and, in the end (2) and (3) are used to calculate the core losses. The magnetic flux density (B_{DUT}) is defined in Fig. 11 and can be calculated using (6) for the ac component and (7)–(8) for the dc component. N_{exc} means the number of turns of excitation winding in the DUT and N_s means the number of turns of sensing winding in the DUT. $v_{DUT}(t)$ is the measured induced voltage on DUT. Care must be taken when calculating (3), due to the voltage overshoot at the edge of square wave. The voltage value at the steady-state (flat) area of square wave should be used to calculate the cancellation factor in (3). The voltage spike in Fig. 11 is caused by the parasitic capacitance of the sensing winding and voltage probe. It can influence the measurement result, but, as shown in Section II-B, the added error should be minimum.

Furthermore, it should be acknowledged that (7) may not hold true at all condition. This is due to the hysteretic properties of magnetic materials [43], which makes $B_{DC}(H_{DC})$ also depend on $\hat{B}$. However, if it is assumed that the material in this work operates in the linear region, (7) can still be used. Whenever in doubt, the B to H conversion factor is given in all figures so readers can compare directly in H_{DC}

$$B_{DUT}(t) = \frac{1}{N_s \cdot A_e} \int_0^t v_{DUT}(t)\, dt \tag{6}$$

$$B_{DC} = \mu_0 \cdot \mu_r \cdot H_{DC} \tag{7}$$

$$H_{DC} = \frac{N_{exc} \cdot I_{DC}}{l_e}. \tag{8}$$

A. DC Bias Impact on Loss Curve

The first step to understand the effect of dc bias is to look at the loss curve. Figs. 12 and 13 show the losses density against peak ac flux density ($\hat{B}$) for core A and B, while Figs. 14 and 15 show the losses density against switching frequency (f_{sw}). The diamond points in the figures are measurement points while the line is the result of regression.

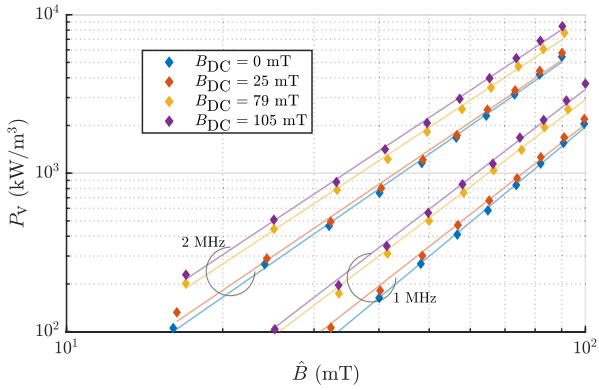

Fig. 13. Core losses (P_v) versus flux density ($\hat{B}$) measured on test core B with different DC flux bias (B_{DC}) and frequency. 1 mT of B_{DC} translates to 0.99 A/m of H_{DC}.

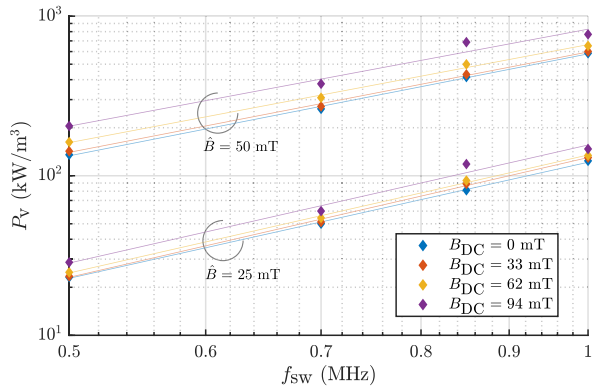

Fig. 14. Core losses (P_v) versus operating (switching) frequency (f_{sw}) measured on test core A with different DC flux bias (B_{DC}) and AC peak flux density ($\hat{B}$). 1 mT of B_{DC} translates to 0.53 A/m of H_{DC}.

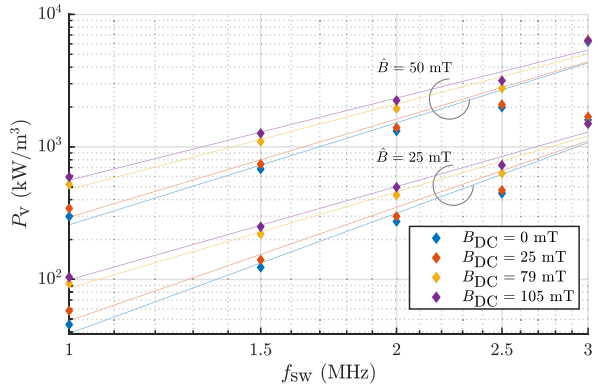

Fig. 15. Core losses (P_v) versus operating (switching) frequency (f_{sw}) measured on test core B with different DC flux bias (B_{DC}) and AC peak flux density ($\hat{B}$). 1 mT of B_{DC} translates to 0.99 A/m of H_{DC}.

The influence of dc bias (B_{DC}) on P_v versus $\hat{B}$ can be seen in Figs. 12 and 13. At low dc bias, the losses increase is relatively small. However, after the dc bias reaches a certain value, the losses increase starts to be significant. For example, at 500 kHz and $\hat{B} = 50$ mT in core A, the losses increase at 33 mT bias is only 5.3%, but at 62 mT bias, the increase becomes 20% and at 94 mT 51.4%. For core B at 1 MHz and $\hat{B} = 50$ mT, the trend

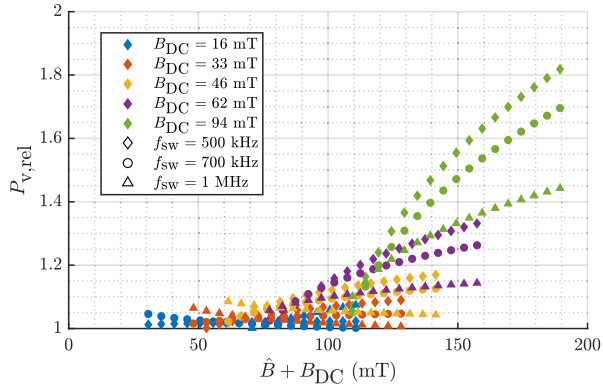

Fig. 16. Relative core losses ($P_{v,rel}$) versus peak total flux density ($\hat{B} + B_{DC}$) at different DC bias and frequency for test core A. 1 mT of B_{DC} translates to 0.53 A/m of H_{DC}.

is similar but at a different level. With 25 mT bias, the increase is 15.1%, but with 79 mT it becomes 75%.

At a single frequency, the measured losses points still follow a straight regression line in logarithmic scale, even after dc bias is applied. This suggests that $P_v \propto \hat{B}^{\beta}$ relation still hold with dc bias. It is also observed that there is a slight shift in the regression line slope. This may suggest a shift in the β parameter. We also see this slope shift is less pronounced in core B, compared to core A. A more detailed modeling is presented in Section IV.

Figs. 14 and 15 show the influence of dc bias (B_{DC}) on P_v versus f_{sw} curve. A similar observation can be found where, again, as the dc bias increases, the loss density also increases. For test core A, the dc bias seems to offset the loss density curve, as can be seen in Fig. 14. Although not very obvious, we can also observe the $P_v \propto f_{sw}^{\alpha}$ relation. The shift in α parameter is not likely for core A, since the curve gradient stays almost the same. Meanwhile for core B, the measurement result suggest a shift in the α parameter. The reason is that the dc bias not only offsets the curve, but also changes the regression line slope in Fig. 15. At $f_{sw} > 2$ MHz, the dc bias effect becomes less predictable in core B. At 3 MHz, the loss increase is almost unnoticeable. This can be caused by the newfound characteristic of the magnetic core, which will be elaborated in the following section.

B. Relative Core Losses Increase

This section will try to answer when the dc bias starts to have significant effect to the core losses. It is also chosen to quantify the dc bias using B field instead of H field. This selection enables magnetic core performance comparison across different permeability value. Although, at the beginning of this section it was noted that throughout this section, the relative core losses increase ($P_{v,rel}$) is calculated by dividing the losses at a certain dc bias with the losses at no bias condition, as shown in the following:

$$P_{v,rel} = \frac{P_{Fe,DC}}{P_{Fe,0}} = \frac{E_{Fe,DC}(f_{sw}, \hat{B}, B_{DC}) \cdot f_{sw}}{E_{Fe,0}(f_{sw}, \hat{B}) \cdot f_{sw}}. \quad (9)$$

Fig. 16 shows for core A when the dc bias impact becomes significant. The sum of ac and dc component of B field is taken

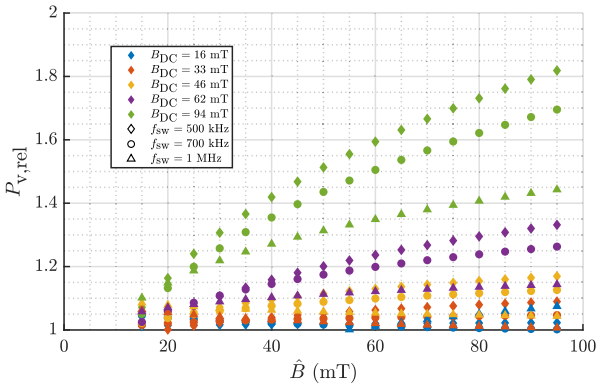

Fig. 17. Relative core losses ($P_{v,rel}$) versus peak AC flux density ($\hat{B}$) at different DC bias and frequency for test core A. 1 mT of B_{DC} translates to 0.53 A/m of H_{DC}.

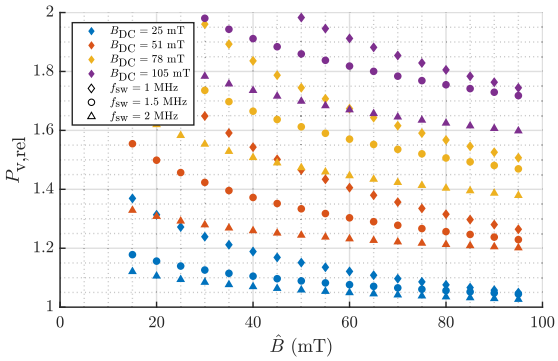

Fig. 19. Relative core losses ($P_{v,rel}$) versus peak AC flux density ($\hat{B}$) at different DC bias and frequency for test core B. 1 mT of B_{DC} translates to 0.99 A/m of H_{DC}.

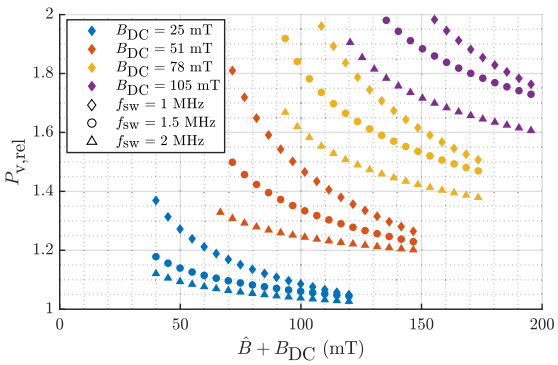

Fig. 18. Relative core losses ($P_{v,rel}$) versus peak total flux density ($\hat{B} + B_{DC}$) at different DC bias and frequency for test core B. 1 mT of B_{DC} translates to 0.99 A/m of H_{DC}.

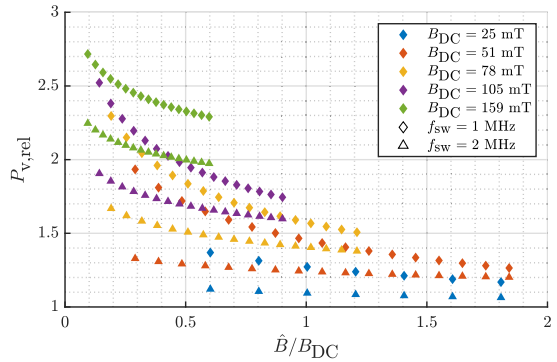

Fig. 20. Relative core losses ($P_{v,rel}$) versus flux density ratio ($\hat{B}/B_{DC}$) at different DC bias and frequency for test core B. 1 mT of B_{DC} translates to 0.99 A/m of H_{DC}.

as the X axis to show if there is a relation between peak flux density and the relative losses increase. The increase starts to become significant, i.e., more than 20%, when the total B is above 100 mT. This can be seen by looking at the measurement points upper envelope. However, for $B_{DC} < 50$ mT, the increase stays low even when the sum is above 100 mT. It means the dc bias magnitude still plays a role in determining the increase.

Furthermore, different operating frequency brings different impact. The higher frequency seems to create lower relative increase, as can be seen by comparing 1 MHz and 500 kHz points in Fig. 16. This behavior indicates that $E_{Fe,0}$ and $E_{Fe,DC}$ in (9) are a function of frequency too. If it is not, $P_{v,rel}$ would show the same value at different frequency. This is in line with the well-known Steinmetz equation, where the loss $P_v \propto f_{sw}^{\alpha}$ and $\alpha > 1$. On the other hand, explaining the physical origin of this behavior would require deep analysis into micromagnetism topic, which is beyond the scope of this article.

A similar observation can be found in Fig. 17, where data points are plotted only against the ac component $\hat{B}$. It also shows that the relative increase ($P_{v,rel}$) becomes higher as $\hat{B}$ increases, which can be caused by bigger hysteresis loop area increase at higher $\hat{B}$.

In test core B, the trend and relationship are less straightforward. Fig. 18 shows the relation between total B field and the relative losses increase. The measurement points are more widespread than core A. Contrary to core A behavior, the relative loss increase is lower as the total flux increases, for a certain B_{DC} and f_{sw}. This trend applies to all tested frequency and dc bias for core B. The dc bias magnitude also determines the relative increase and here the loss gain is more pronounced, e.g., at 1 MHz the $P_{v,rel}$ is close to two when $\hat{B} + B_{DC}$ is around 100 mT and $B_{DC} = 78$ mT. This is a steep increase and designers should take care of it when designing the magnetic components.

Meanwhile, the impact of frequency is quite similar to core A. The higher frequency creates a lower relative loss increase. When data points are plotted only against the ac component $\hat{B}$, Fig. 19 is obtained. It also shows that the relative increase ($P_{v,rel}$) becomes lower as $\hat{B}$ increases. This behavior is different from core A.

The same data in Fig. 18 can also be presented in a different way as in Fig. 20. The B ratio of ac and dc components ($\hat{B}/B_{DC}$) is plotted against loss increase. This is done to check if a different characteristics of the core losses can be seen. Nevertheless, a similar observation is found. The B_{DC} is the main controlling factor for $P_{v,rel}$. The $\hat{B}/B_{DC}$ ratio plays a smaller role, although it still has an impact, i.e., higher ratio makes lower loss increase. This observation reflects a complex physics behind the core losses phenomenon.

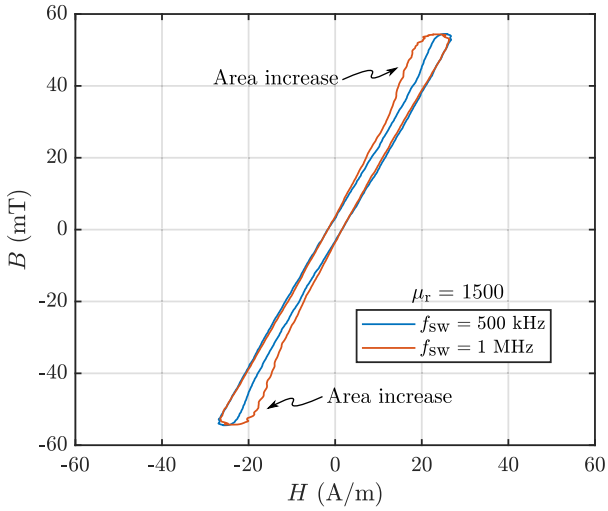

Fig. 21. *B–H* loop at different frequency for test core A. No DC bias applied.

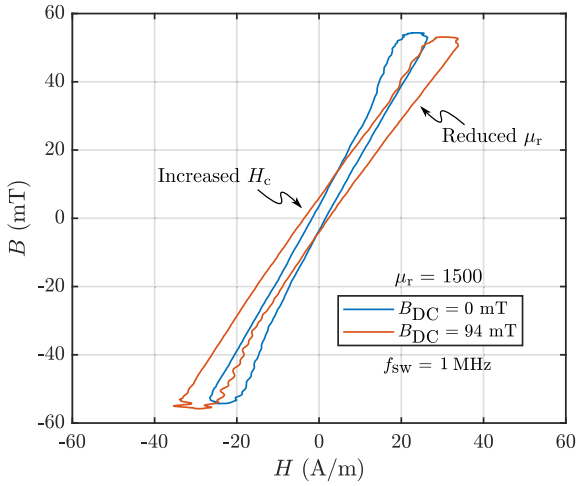

Fig. 23. *B–H* loop at different DC bias for test core A. Only the AC component is plotted.

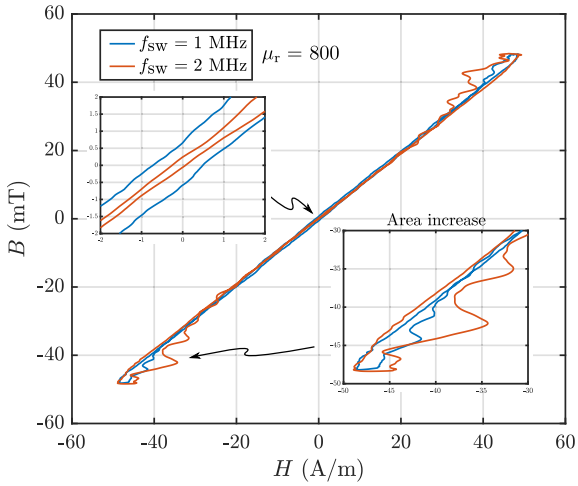

Fig. 22. *B–H* loop at different frequency for test core B. No DC bias applied.

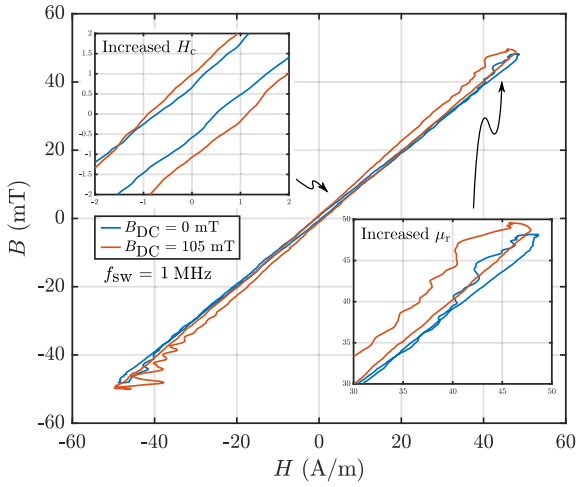

Fig. 24. *B–H* loop at different DC bias for test core B. Only the AC component is plotted.

C. Impact on B–H Curve

Apart from measuring core losses, we can also measure the magnetic material *B–H* loop using the same setup. The B field is calculated using (6) from voltage measurement and H field using (8), but with instantaneous current instead of dc current. The *B–H* loop area reflects the hysteresis loss components of a magnetic core. The area equals to the lost energy per magnetization cycle. Although possible, it is hard to calculate the hysteresis losses accurately, given the delays and parasitic in the setup. Hence, the analysis in this section is more of a qualitative nature.

First, we look at the classical behavior of *B–H* loop for different material at changing frequency. Figs. 21 and 22 present the loop for core A and B, respectively. From literature and previous works [22], [29], [44], it is expected that the *B–H* loop area increases as frequency increases. This is seen in both core A and B. In core A, the major area increase appears near the peak B point, both at positive and negative. This is when the reversal of magnetic domain magnetization begins. As switching frequency increases, the delay in magnetization reversal makes the B value falls slower [1], compared to the switching period. In core B, the situation is similar except with a slightly different *B–H* loop shape. The area increase also appears in core B. On the other hand, core B exhibits lower coercivity when frequency increases. It is a different case compared to core A, where the coercivity stays almost the same at both frequencies. Coercivity can be seen near $B \approx 0$. Hence, it shows a different behavior of magnetic material with different relative permeability level.

Second, we look at the dc bias impact on *B–H* loop. Figs. 23 and 24 present the curve change for core A and B, respectively. The first effect is the shift of μ_r, as can be seen by the *B–H* curve slope. For test core A, increasing dc bias makes μ_r value lower. Meanwhile, for core B, increasing dc bias brings the opposite effect. The second effect is the *B–H* loop area increase, which leads to the loss increase found in the previous section. The area increase can be observed in two places. One place is near the magnetization reversal or peak B point. The second place is found by looking at the coercivity (H_c). In both Figs. 23 and 24, we can see the increase in H_c (equals to ΔH when

$B = 0$). This behavior can be explained by the minor loop behavior of magnetic materials [45]. Unfortunately, there is not enough literature, which can bridge the magnetism behavior from the micro to macro level to explain this thoroughly. Nevertheless, the observation on *B–H* loop agrees with the loss increase finding due to added dc bias.

IV. Modeling DC Bias on Core Loss

This section does not try to propose a whole new model to predict core losses. Instead, we will see if the available models can still accurately predict core losses from the measurement results generated in this work, particularly this means incorporating the impact of dc bias in core losses prediction. Out of many previously proposed core losses modeling [8], [10], [13], [24], [28], the method in [24] and one similar to [46] will be used in the following analysis. The two methods represent two different nature of modeling approach. The first one is based more on a traditional formula method with multiple parameters, while the latter is based more on machine learning approach.

A. Empirical Formula: IGSE With SPG

The main advantage of using analytical formula in modeling core losses is getting the insight into the physics behind the losses mechanism. The explicit formula shows the user which parameters are affecting the core losses. Hence, giving some understanding of the core losses behavior.

Since in power electronics the flux (B) waveform is commonly not sinusoidal, the established improved generalized Steinmetz Equation (*iGSE*) method [13] can be adopted to calculate the core losses. However, this modeling does not include dc bias effect. Therefore, it needs to be modified with other techniques. The Steinmetz Premagnetization Graph (*SPG*) method [24] can incorporate the dc bias effect without changing the original equation so, it is used in this work. The iGSE formula when applied to triangular flux waveform is reduced to the form in (10). Then, with SPG method, α, β, and k_i will be modified following (11), which incorporates the dependence on dc bias (B_DC).

The appropriate coefficients of SPG matrix [first term of right hand side in (11)] needs to be found in order to extract the dependence. This is done by solving a curve fitting problem. A least square error algorithm has been implemented that fits the calculated curve with measured data by minimizing the relative error. Despite the fourth-order polynomial used here, the order can be varied if the curve fitting result does not generate a good prediction accuracy. In this work, the fourth-order proves to be sufficient. The coefficients in (12) can also be found by curve fitting, but more measurement data, especially at different frequency, will be needed. This is because in *SPGi* method (explained below), the α parameter, which determines the frequency influence, also changes with B_DC. Common computing software such as MATLAB or Octave has some built-in application to perform the curve fitting task

$$P_{\mathrm{v,iGSE,tri}} = k_\mathrm{i} \cdot (2f)^{\alpha} \cdot (\Delta B)^{\beta} \tag{10}$$

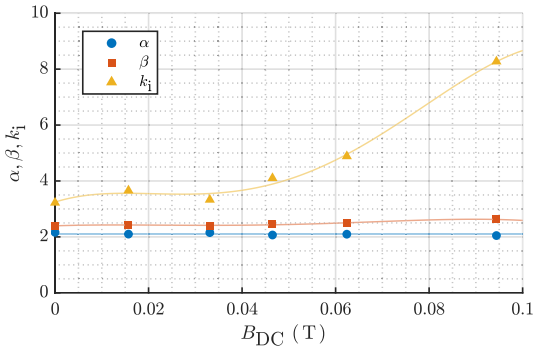

Fig. 25. Steinmetz premagnetization Graph for test core A. The k_i value is scaled down by 10^4 to increase graph readability. The data points are measurement result and the line is curve-fitting result.

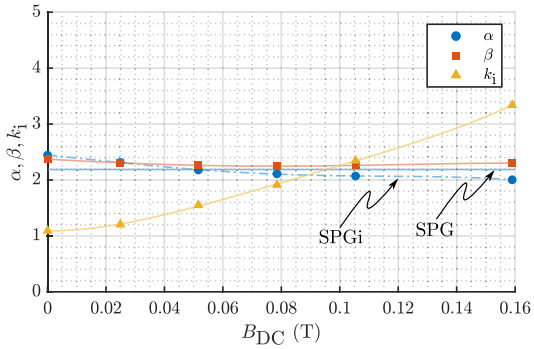

Fig. 26. Steinmetz premagnetization Graph for test core B. The k_i value is scaled down by 10^4 to increase graph readability. The data points are measurement result and the line is curve-fitting result.

$$\begin{bmatrix} \alpha \\ \beta \\ k_\mathrm{i} \end{bmatrix} = \begin{bmatrix} \alpha_0 & 0 & 0 & 0 & 0 \\ \beta_0 & p_{\beta 1} & p_{\beta 2} & p_{\beta 3} & p_{\beta 4} \\ k_{\mathrm{i}0} & p_{ki1} & p_{ki2} & p_{ki3} & p_{ki4} \end{bmatrix} \cdot \begin{bmatrix} 1 \\ B_\mathrm{DC} \\ B_\mathrm{DC}^2 \\ B_\mathrm{DC}^3 \\ B_\mathrm{DC}^4 \end{bmatrix} \tag{11}$$

$$\begin{bmatrix} \alpha \\ \beta \\ k_\mathrm{i} \end{bmatrix} = \begin{bmatrix} \alpha_0 & p_{\alpha 1} & p_{\alpha 2} & p_{\alpha 3} & p_{\alpha 4} \\ \beta_0 & p_{\beta 1} & p_{\beta 2} & p_{\beta 3} & p_{\beta 4} \\ k_{\mathrm{i}0} & p_{ki1} & p_{ki2} & p_{ki3} & p_{ki4} \end{bmatrix} \cdot \begin{bmatrix} 1 \\ B_\mathrm{DC} \\ B_\mathrm{DC}^2 \\ B_\mathrm{DC}^3 \\ B_\mathrm{DC}^4 \end{bmatrix}. \tag{12}$$

Following the mentioned procedure, the SPG dependence graph can be obtained. This is shown in Figs. 25 and 26 for core A and B, respectively. The data points are measurement result and the line is curve-fitting result. For core A, the α and β parameters stay relatively constant over the whole B_DC range. Meanwhile, k_i fluctuates smoothly at low B_DC and increases quite steeply after $B_\mathrm{DC} > 50$ mT. This observation aligns with the analysis in Section III-B, where the relative losses gain rises quickly after a certain B_DC values.

For core B, the k_i increases steadily from low B_DC and shows an almost linear relation to B_DC. The β parameters has a slight decline from low to mid B_DC, while α shows a decreasing trend toward higher B_DC. The conventional SPG prediction

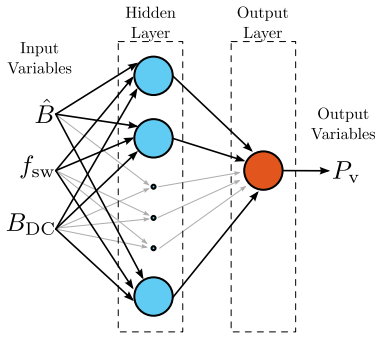

Fig. 27. Structure of ANN for core losses estimation with three inputs, one output, one hidden layer, and one output layer.

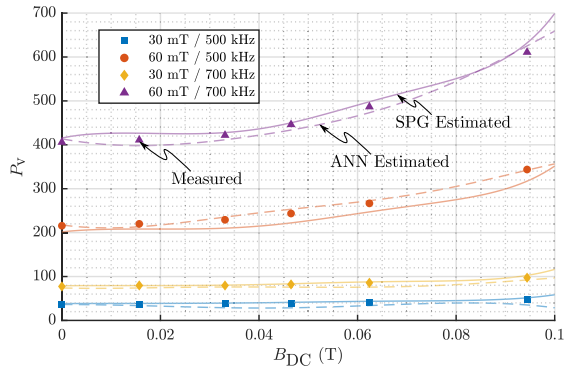

Fig. 28. Core loss density (P_v) estimation of test core A. The scatter points are measurement data while the curves are prediction result from SPG method (solid lines) and ANN method (dashed lines).

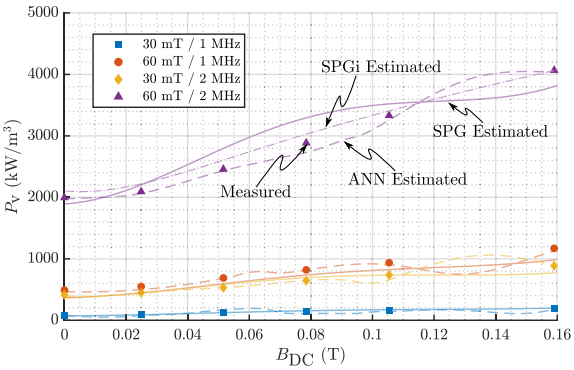

Fig. 29. Core loss density (P_v) estimation of test core B. The scatter points are measurement data while the curves are prediction result from SPG method (solid lines) and ANN method (dashed lines).

cannot capture the α shift because (11) assumes a constant α value. This assumption may not hold true anymore after seeing the measurement result in Figs. 18 and 20. Therefore, a new formulation of SPG matrix can be built by replacing the zeros in (11) with $p_{\alpha i}$. The new formula is given in (12). With this new modification, a better fitting for core B will be achieved. This new modification is denoted as *SPGi* in Fig. 26 and proven to give more accurate loss prediction.

After having the SPG coefficients matrix, (10) is used to calculate the core losses in the presence of dc bias. The results are shown in Figs. 28 and 29 for core A and B, respectively, with several different $\hat{B}$ and f_{sw} values. The measurement points are also shown to compare the loss prediction and measurement. The iGSE + SPG method appears to be reasonably accurate in the whole B_{DC} range for core A. The accuracy at low $\hat{B}$ (30 mT) is better than at high $\hat{B}$ (60 mT) in core A. For core B, this method loses accuracy at high $\hat{B}$ and high f_{sw}, as can be seen in Fig. 29. However, with the proposed *SPGi* modification, the accuracy is improved. The maximum error at 2 MHz is reduced from 14% to 6.7%, while the maximum overall error is down from 25% to 20%. It is worth to note that this maximum error happens at low $\hat{B}$ and f_{sw} value, where a small deviation means higher error percentage. Meanwhile for core A, the overall maximum error is only 8.8%.

B. Machine Learning: ANN

Artificial neural network (ANN) is the most popular implementation of supervised machine learning methods. It has the ability to predict values (regression) or categories (classification) from labeled training data (input–output pairs). In power electronic systems, ANN has been used for control strategies [47], [48], fault diagnosis [49], and also component design [38]. Here, ANN will be used to create a core loss prediction model. The core loss is nonlinearly correlated to the excitation frequency, amplitude, and dc bias, which can be hardly captured by the traditional equation-based methods. Hence, the ANN is expected to help in this case.

The selected ANN structure is shown in Fig. 27, which can be classified as multilayer perceptron (MLP) type. The ANN features a two-layer feed-forward network with sigmoid hidden neurons (in the hidden layer) and linear output neurons (in the output layer). Since the only output variable in this problem is the core losses (P_v), only one neuron is in the output layer. Meanwhile, the number of neurons in the hidden layer can be tuned. A too low number will make value prediction not accurate, while a too high number can lead to overfitting [50]. In this work, ten hidden layer neurons prove to be sufficient. The network will be trained with Levenberg–Marquardt backpropagation algorithm [51], [52] in MATLAB platform. The ANN for core A and B are trained separately, with 777 measurement samples for core A and 918 samples for core B. The splitting between the training set and the test set is 80% and 20% in all cases.

After the ANN is built and trained, it is tested to predict core losses with arbitrary inputs. The result is plotted in Figs. 28 and 29 as a curve. The real measurement points are also plotted to compare it with the ANN prediction. The test core A prediction by ANN shows a good performance as can be seen in Fig. 28. At 60 mT and 500 kHz, it even gives a better matching than SPG method. For core B, the result is less satisfactory. Although the ANN gives better prediction at 60 mT and 2 MHz, it displays an overfitting behavior at 60 mT/1 MHz and 30 mT/2 MHz condition. Nevertheless, the deviation still falls in the reasonable range. The overall maximum error for core A and B are 27% and 37%, respectively. Again, these maximum errors happen at low P_v range, where it is sensitive to small deviation. If the 30 mT/500 kHz and 30 mT/1 MHz series are excluded, the overall maximum errors become 11.6% and 10.9% for core A

and B. The average errors when the trained model is tested with dataset in Figs. 28 and 29 are 7.2% for core A and 6.7% for core B. The ANN shows a rather simple yet powerful approach to core losses modeling.

V. Conclusion

This article investigates magnetic core losses under square wave excitation with superimposed dc bias. The frequency of interest is from 500 kHz up to 3 MHz and the tested material is MnZn ferrite with nominal relative permeability (μ_r) of 1500 and 800, which are the state-of-the-art for power electronics application. Section II describes the core losses measurement setup. The mutual inductance neutralization method is used to minimize the measurement error. The measurement results are presented in Section III. The dc bias essentially generates an offset to the loss curve, creating higher losses. It was also seen that there is a shift in Steinmetz parameter, especially β, after bias is applied. Nevertheless, the proportionality $P_v \propto \hat{B}^{\beta}$ and $P_v \propto f_{sw}^{\alpha}$ still hold. Section IV attempts to model the core losses behavior by using two different approach: Steinmetz Premagnetization Graph (SPG) and artificial neural network (ANN). The SPG method modifies the Steinmetz parameter using a polynomial function of the dc bias and the model has a maximum error percentage of 25% in our test. With the proposed SPGi modification, this error is brought down to 20%. Meanwhile, the ANN method relies on neurons, which were trained by the measurement data beforehand. The ANN model has a maximum error percentage of 37% in our test. In a nutshell, this article clarifies ferrite core losses behavior in the mentioned frequency range and quantitatively analyzes the possible models. As a further step, the models and measurement data can be expanded, as in [46] and [53], and shared to be used with other magnetic designers.

Appendix A
Measurement Setup and DUT Implementation

The real life setup of the measurement system is shown in Fig. 30. A high-frequency GaNFET half-bridge is used as the square-wave generator. The circuit is able to generate up to 100 V amplitude at 5-MHz switching frequency. I_{DC} is implemented using a current controlled dc e-load.

Meanwhile, the DUTs for measurement are shown in Fig. 31. Single turn windings are used to minimize the parasitic capacitance. The magnetizing and leakage inductance values are given in Figs. 32 and 33, along with the reference/compensation element's values. This shows the range of inductance used in this work and justifies the parameters used in error calculation in Section II-B. The shaded area represents the range of frequency, where the DUT is tested.

Appendix B
Error Due to Capacitances

The derivation of errors due to the parasitic capacitances are given below. The considered circuit is shown in Fig. 34, which is then simplified to Fig. 35 with part of the equivalent circuit in

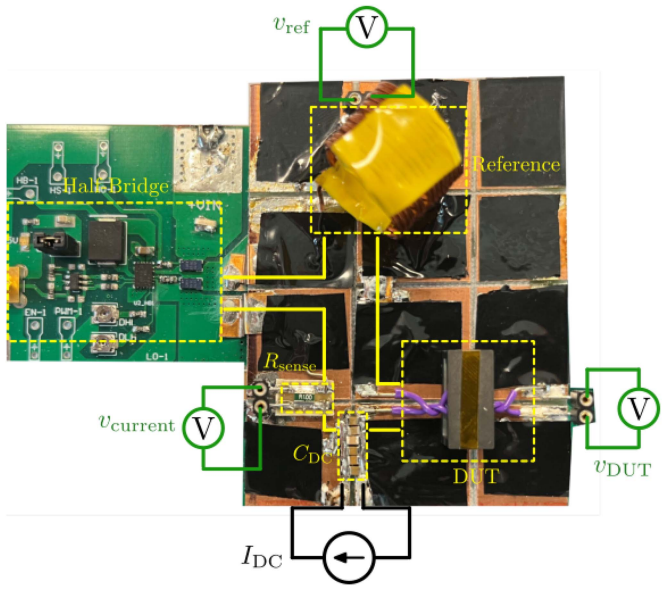

Fig. 30. Implemented core loss measurement setup.

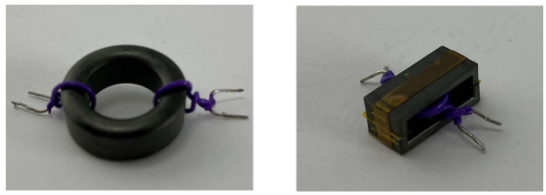

(a) (b)

Fig. 31. Photos of DUTs: core A (a) and core B (b). The specifications are given in Table II.

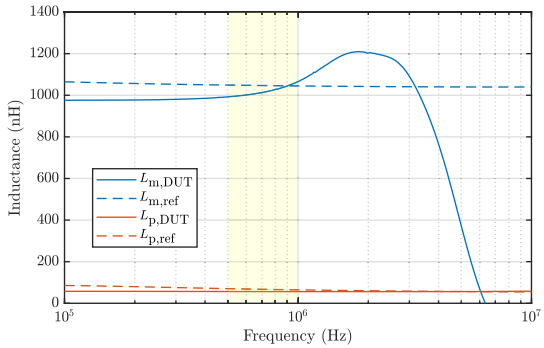

Fig. 32. Measured magnetizing and stray inductance of DUT core A.

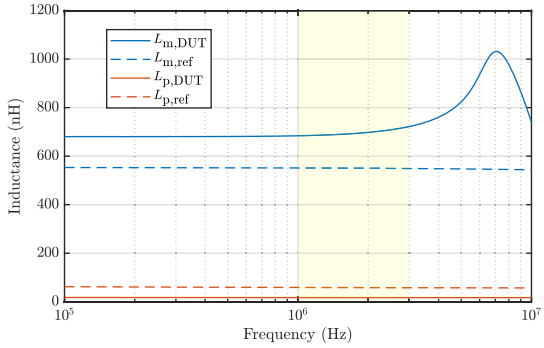

Fig. 33. Measured magnetizing and stray inductance of DUT core B.

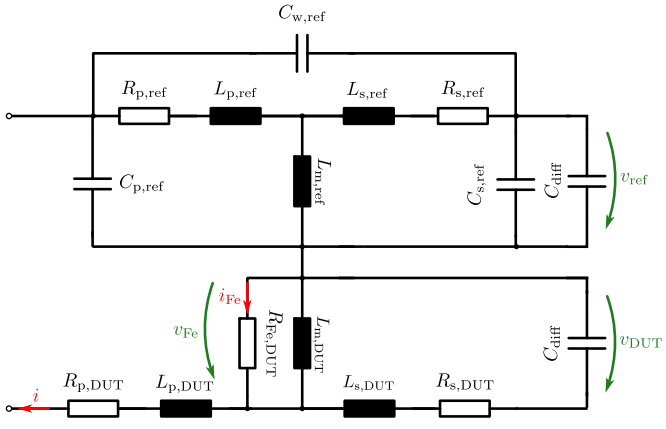

Fig. 34. Considered circuit for calculating the error caused by the parasitic capacitance elements.

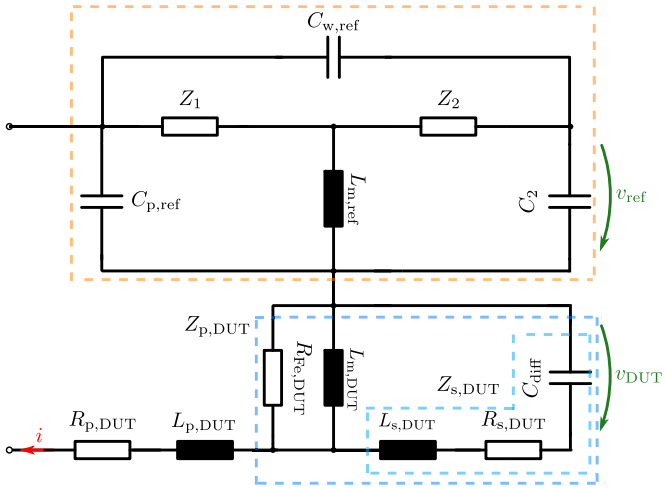

Fig. 35. Considered circuit after the simplification of the reference elements. Dashed blue boxes show the equivalent impedance definition.

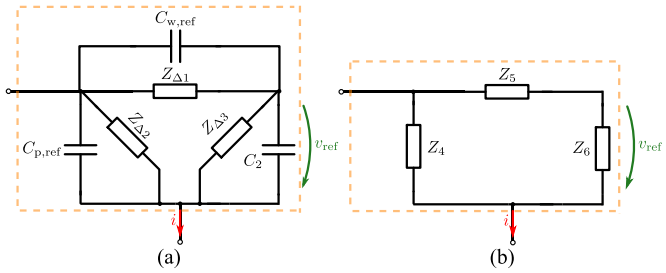

Fig. 36. Equivalent circuit of the elements in dashed orange box.

Fig. 36. The error is calculated by finding the value of ΔP. It is based on P_{act} and P_{meas} calculation

$$\Delta P = \frac{P_{\mathrm{meas}} - P_{\mathrm{act}}}{P_{\mathrm{act}}}$$

$$P_{\mathrm{act}} = \frac{1}{T_{\mathrm{sw}}}\left(\int_0^{T_{\mathrm{sw}}} v_{\mathrm{Fe}}(t)\cdot i_{\mathrm{Fe}}(t)\,dt\right)$$

$$= \frac{1}{2}\cdot \mathrm{Re}[\mathbf{V}_{\mathrm{Fe}}\cdot \mathbf{I}_{\mathrm{Fe}}^{*}] = \frac{1}{2}\cdot\frac{V_{Fe}^2}{R_{\mathrm{Fe}}}$$

$$P_{\mathrm{meas}} = \frac{1}{T_{\mathrm{sw}}}\left(\int_0^{T_{\mathrm{sw}}} v_{\mathrm{DUT}}(t)\cdot i(t)\,dt - \frac{1}{k}\int_0^{T_{\mathrm{sw}}} v_{\mathrm{ref}}(t)\cdot i(t)\,dt\right)$$

$$= \frac{1}{2}\cdot \mathrm{Re}[\mathbf{V}_{\mathrm{DUT}}\cdot \mathbf{I}^{*}] - \frac{1}{k}\cdot\frac{1}{2}\cdot \mathrm{Re}[\mathbf{V}_{\mathrm{ref}}\cdot \mathbf{I}^{*}].$$

The required phasor variables are derived in the following.

$$\mathbf{V}_{\mathrm{DUT}} = \frac{1/j\omega C_{\mathrm{diff}}}{1/j\omega C_{\mathrm{diff}} + j\omega L_{\mathrm{s,DUT}} + R_{\mathrm{s,DUT}}}\cdot \mathbf{V}_{\mathrm{Fe}}$$

$$\mathbf{I} = \frac{\mathbf{V}_{\mathrm{Fe}}}{\mathbf{Z}_{\mathrm{p,DUT}}}$$

$$[\mathbf{V}_{\mathrm{DUT}}\cdot \mathbf{I}^{*}] = \frac{V_{Fe}^2}{\omega C_{\mathrm{diff}}\cdot Z_{s,DUT}\cdot Z_{p,DUT}} -\pi/2 - \theta_{Z_{s,dut}} + \theta_{Z_{p,dut}}$$

$$k = \frac{L_{\mathrm{m,ref}}}{L_{\mathrm{m,DUT}}}$$

$$C_2 = C_{\mathrm{s}} + C_{\mathrm{d}}$$

$$\mathbf{Z}_1 = R_{\mathrm{p,ref}} + j\omega L_{\mathrm{p,ref}}$$

$$\mathbf{Z}_2 = R_{\mathrm{s,ref}} + j\omega L_{\mathrm{s,ref}}$$

$$\mathbf{Z}_{\Delta 1} = \frac{\mathbf{Z}_1\cdot\mathbf{Z}_2 + \mathbf{Z}_1\cdot j\omega L_{\mathrm{m,ref}} + \mathbf{Z}_2\cdot j\omega L_{\mathrm{m,ref}}}{j\omega L_{\mathrm{m,ref}}}$$

$$\mathbf{Z}_{\Delta 2} = \frac{\mathbf{Z}_1\cdot\mathbf{Z}_2 + \mathbf{Z}_1\cdot j\omega L_{\mathrm{m,ref}} + \mathbf{Z}_2\cdot j\omega L_{\mathrm{m,ref}}}{\mathbf{Z}_2}$$

$$\mathbf{Z}_{\Delta 3} = \frac{\mathbf{Z}_1\cdot\mathbf{Z}_2 + \mathbf{Z}_1\cdot j\omega L_{\mathrm{m,ref}} + \mathbf{Z}_2\cdot j\omega L_{\mathrm{m,ref}}}{\mathbf{Z}_1}$$

$$\mathbf{V}_{\mathrm{ref}} = \mathbf{I}\cdot\frac{\mathbf{Z}_4\cdot\mathbf{Z}_6}{\mathbf{Z}_4+\mathbf{Z}_5+\mathbf{Z}_6}$$

$$[\mathbf{V}_{\mathrm{ref}}\cdot \mathbf{I}^{*}] = \frac{V_{Fe}^2}{Z_{p,DUT}^2}\cdot\frac{\mathbf{Z}_4\cdot\mathbf{Z}_6}{\mathbf{Z}_4+\mathbf{Z}_5+\mathbf{Z}_6}.$$

REFERENCES

[1] S. Blundell, *Magnetism in Condensed Matter*, 1st ed. Oxford, U.K.: Oxford Univ. Press, 2014.

[2] E. C. Snelling, *Soft Ferrites, Properties and Application*, 2nd ed. New York, NY, USA: Butterworths, 1988.

[3] W. Roshen, "Ferrite core loss for power magnetic components design," *IEEE Trans. Magn.*, vol. 27, no. 6, pp. 4407–4415, Nov. 1991.

[4] R. M. Bozorth, *Ferromagnetism*. Piscataway, NJ, USA: IEEE Press, 1993.

[5] H. J. Williams, W. Shockley, and C. Kittel, "Studies of the propagation velocity of a ferromagnetic domain boundary," *Phys. Rev.*, vol. 80, no. 6, pp. 1090–1094, 1950. [Online]. Available: https://link.aps.org/doi/10.1103/PhysRev.80.1090

[6] G. Bertotti, "General properties of power losses in soft ferromagnetic materials," *IEEE Trans. Magn.*, vol. 24, no. 1, pp. 621–630, Jan. 1988.

[7] I. D. Mayergoyz and G. Friedman, "Generalized Preisach model of hysteresis," *IEEE Trans. Magn.*, vol. 24, no. 1, pp. 212–217, Jan. 1988.

[8] I. D. Mayergoyz, "Dynamic Preisach models of hysteresis," *IEEE Trans. Magn.*, vol. 24, no. 6, pp. 2925–2927, Nov. 1988.

[9] C. P. Steinmetz, "On the law of hysteresis," *Trans. Amer. Inst. Elect. Eng.*, vol. 9, no. 1, pp. 1–1892.

[10] M. Albach, T. Durbaum, and A. Brockmeyer, "Calculating core losses in transformers for arbitrary magnetizing currents a comparison of different approaches," in *Proc. PESC Record. 27th Annu. IEEE Power Electron. Specialists Conf.*, 1996, pp. 1463–1468.

[11] J. Reinert, A. Brockmeyer, and R. De Doncker, "Calculation of losses in ferro- and ferrimagnetic materials based on the modified steinmetz equation," *IEEE Trans. Ind. Appl.*, vol. 37, no. 4, pp. 1055–1061, Jul./Aug. 2001.
[12] J. Li, T. Abdallah, and C. Sullivan, "Improved calculation of core loss with nonsinusoidal waveforms," in *Proc. Conf. Rec. IEEE Ind. Appl. Conf. 36th IAS Annu. Meeting (Cat. No.01CH37248)*, 2001, pp. 2203–2210.
[13] K. Venkatachalam, C. Sullivan, T. Abdallah, and H. Tacca, "Accurate prediction of ferrite core loss with nonsinusoidal waveforms using only steinmetz parameters," in *Proc. IEEE Workshop Comput. Power Electron.*, 2002, pp. 36–41.
[14] J. Muhlethaler, J. Biela, J. W. Kolar, and A. Ecklebe, "Improved core-loss calculation for magnetic components employed in power electronic systems," *IEEE Trans. Power Electron.*, vol. 27, no. 2, pp. 964–973, Feb. 2012.
[15] T. Shimizu and S. Iyasu, "A practical iron loss calculation for AC filter inductors used in PWM inverters," *IEEE Trans. Ind. Electron.*, vol. 56, no. 7, pp. 2600–2609, Jul. 2009.
[16] S. Iyasu, T. Shimizu, and K. Ishii, "A novel iron loss calculation method on power converters based on dynamic minor loop," in *Proc. Eur. Conf. Power Electron. Appl.*, 2005, pp. 9–18.
[17] W. A. Roshen, "A practical, accurate and very general core loss model for nonsinusoidal waveforms," *IEEE Trans. Power Electron.*, vol 22, no. 1, pp. 30–40, Jan. 2007.
[18] P. Papamanolis, T. Guillod, F. Krismer, and J. W. Kolar, "Transient calorimetric measurement of ferrite core losses up to 50 MHz," *IEEE Trans. Power Electron.*, vol. 36, no. 3, pp. 2548–2563, Mar. 2021.
[19] A. Van den Bossche, V. Valchev, and G. Georgiev, "Measurement and loss model of ferrites with non-sinusoidal waveforms," in *Proc. IEEE 35th Annu. Power Electron. Specialists Conf. (Cat. No.04CH37551)*, 2004, pp. 4814–4818.
[20] W. G. Hurley, T. Merkin, and M. Duffy, "The performance factor for magnetic materials revisited: The effect of core losses on the selection of core size in transformers," *IEEE Power Electron. Mag.*, vol. 5, no. 3, pp. 26–34, Sep. 2018.
[21] B. N. Sanusi and Z. Ouyang, "Magnetic core losses under square-wave excitation and DC bias in high frequency regime," in *Proc. IEEE Appl. Power Electron. Conf. Expo.*, 2022, vol. 3, pp. 633–639.
[22] A. Brockmeyer, "Experimental evaluation of the influence of DC-premagnetization on the properties of power electronic ferrites," in *Proc. Appl. Power Electron. Conf.*, 1996, pp. 454–460.
[23] C. Baguley, B. Carsten, and U. Madawala, "The effect of DC bias conditions on ferrite core losses," *IEEE Trans. Magn.*, vol. 44, no. 2, pp. 246–252, Feb. 2008.
[24] J. Muhlethaler, J. Biela, J. W. Kolar, and A. Ecklebe, "Core losses under the DC bias condition based on steinmetz parameters," *IEEE Trans. Power Electron.*, vol. 27, no. 2, pp. 953–963, Feb. 2012.
[25] A. J. Hanson, J. A. Belk, S. Lim, C. R. Sullivan, and D. J. Perreault, "Measurements and performance factor comparisons of magnetic materials at high frequency," *IEEE Trans. Power Electron.*, vol. 31, no. 11, pp. 7909–7925,Nov. 2016.
[26] M. Mu, Q. Li, D. J. Gilham, F. C. Lee, and K. D. Ngo, "New core loss measurement method for high-frequency magnetic materials," *IEEE Trans. Power Electron.*, vol. 29, no. 8, pp. 4374–4381, Aug. 2014.
[27] D. Hou, M. Mu, F. C. Lee, and Q. Li, "New high-frequency core loss measurement method with partial cancellation concept," *IEEE Trans. Power Electron.*, vol. 32, no. 4, pp. 2987–2994, Apr. 2017.
[28] E. Stenglein and T. Durbaum, "Core loss model for arbitrary excitations with DC bias covering a wide frequency range," *IEEE Trans. Magn.*, vol. 57, no. 6, Jun. 2021, Art. no. 6302110.
[29] E. Stenglein, M. Albach, and T. Durbaum, "Separation of magnetic flux density trajectories into subloops for the prediction of hysteresis loss," in *Proc. 22nd Eur. Conf. Power Electron. Appl.*, 2020, pp. 1–10.
[30] F. Dong Tan, J. Vollin, and S. Cuk, "A practical approach for magnetic core-loss characterization," *IEEE Trans. Power Electron.*, vol. 10, no. 2, pp. 124–130, Mar. 1995.
[31] C. Baguley, U. Madawala, and B. Carsten, "A new technique for measuring ferrite core loss under DC bias conditions," *IEEE Trans. Magn.*, vol. 44, no. 11, pp. 4127–4130, Nov. 2008.
[32] Itech Electronic Co., Ltd., "Programmable DC Electronic Load Series IT8800." 2022. [Online]. Available: https://www.itechate.com/en/product/dc-electronic-load/IT8800.html
[33] Testec GmbH, "Instruction Manual TT-SI 9001/TT_SI 9002." 2022. [Online]. Available: https://www.testec.de/en/products/product-categories/differential-probes/
[34] Tektronix Inc., "P6022 Current Probe Instruction Manual." 2022. [Online]. Available: https://www.tek.com/en/datasheet/ac-current-probes
[35] Rohde & Schwarz, "RT-Zxx Standard Passive Probes Specification." 2022. [Online]. Available: https://www.rohde-schwarz.com/cz/products/test-and-measurement/oscilloscope-probes/passive-probes-for-oscilloscopes_63493-73792.html
[36] Susumu, "Metal Foil Low Resistance Chip Resistors - PRL Series." 2022. [Online]. Available: https://www.susumu.co.jp/usa/product/category.php?cid=7?cid=7
[37] P. Papamanolis, T. Guillod, F. Krismer, and J. W. Kolar, "Minimum loss operation and optimal design of high-frequency inductors for defined core and litz wire," *IEEE Open J. Power Electron.*, vol. 1, pp. 469–487, 2020.
[38] T. Guillod, P. Papamanolis, and J. W. Kolar, "Artificial neural network (ANN) based fast and accurate inductor modeling and design," *IEEE Open J. Power Electron.*, vol. 1, pp. 284–299, 2020.
[39] Iwatsu Electric Co Ltd., "B - H Analyzer SY-8218 / SY-8219." 2022. [Online]. Available: https://www.iwatsu-europe.com/en/products/sy/sy8218_sy810_e.html
[40] Ferroxcube Ltd., "Datasheet: 3F46," 2016. [Online]. Available: https://www.ferroxcube.com/en-global/ak_material/index/power_conversion
[41] Hitachi Metals Ltd., "Soft ferrites," 2020. [Online]. Available: http://www.hitachi-metals.co.jp/e/products/elec
[42] TDK Corp., "High-frequency, low-loss ferrite material PC200," 2020. [Online]. Available: https://product.tdk.com/info/en/products/ferrite
[43] E. Stenglein, B. Kohlhepp, D. Kubrich, M. Albach, and T. Durbaum, "GaN-Half-Bridge for core loss measurements under rectangular AC voltage and DC bias of the magnetic flux density," *IEEE Trans. Instrum. Meas.*, vol. 69, no. 9, pp. 6312–6321, Sep. 2020.
[44] M. Lancarotte, C. Goldemberg, and A. d. A. Penteado, "Estimation of FeSi core losses under PWM or DC bias ripple voltage excitations," *IEEE Trans. Energy Convers.*, vol. 20, no. 2, pp. 367–372, Jun. 2005.
[45] D. Jiles, "A self consistent generalized model for the calculation of minor loop excursions in the theory of hysteresis," *IEEE Trans. Magn.*, vol. 28, no. 5, pp. 2602–2604, Sep. 1992.
[46] H. Li, S. R. Lee, M. Luo, C. R. Sullivan, Y. Chen, and M. Chen, "MagNet: A machine learning framework for magnetic core loss modeling," in *Proc. IEEE 21st Workshop Control Model. Power Electron.*. 2020, pp. 1–8.
[47] T. Dragicevic and M. Novak, "Weighting factor design in model predictive control of power electronic converters: An artificial neural network approach," *IEEE Trans. Ind. Electron.*, vol. 66, no. 11, pp. 8870–8880, Nov. 2019.
[48] Q. Xu, T. Dragicevic, L. Xie, and F. Blaabjerg, "Artificial intelligence-based control design for reliable virtual synchronous generators," *IEEE Trans. Power Electron.*, vol. 36, no. 8, pp. 9453–9464, Aug. 2021.
[49] F. Filippetti, G. Franceschini, C. Tassoni, and P. Vas, "Recent developments of induction motor drives fault diagnosis using AI techniques," *IEEE Trans. Ind. Electron.*, vol. 47, no. 5, pp. 994–1004, Oct. 2000.
[50] S. Skansi, *Introduction to Deep Learning: From Logical Calculus to Artificial Intelligence*. Berlin/Heidelberg, Germany: Springer, 2018.
[51] M. Hagan and M. Menhaj, "Training feedforward networks with the marquardt algorithm," *IEEE Trans. Neural Netw.*, vol. 5, no. 6, pp. 989–993, Nov. 1994.
[52] M. Hagan, H. B. Demuth, M. H. Beale, and O. De Jesus, *Neural Network Design*, 2nd ed. Martin Hagan, 2014. [Online]. Available: https://hagan.okstate.edu/NNDesign.pdf
[53] E. Dogariu et al., "Transfer learning methods for magnetic core loss modeling," in *Proc. IEEE 22nd Workshop Control Modelling Power Electron.*, 2021, pp. 1–6.

Bima Nugraha Sanusi (Graduate Student Member, IEEE) received the B.Sc. degree in electrical engineering from Bandung Institute of Technology (ITB), Bandung, Indonesia, in 2015, and the M.Sc. degree in electrical engineering and information technology from the Swiss Federal Institute of Technology (ETH), Zurich, Switzerland, in 2018. He is currently working toward the Ph.D. degree in power electronics with the Power Electronics Group, Technical University of Denmark (DTU), Kongens Lyngby, Denmark.

His current research interests include high-frequency power conversion, integrated magnetics design, magnetic losses measurement and modeling, and highly compact dc–dc converter. He worked as a model based System Engineer with FPT Motorenforschung AG and a Research Assistant with High Power Electronics Laboratory, ETH Zurich, in between his education.

Mr. Sanusi was the recipient of ABB Jurgen Dormann Foundation Scholarship while he was with ITB Bandung and received the Master Scholarship Program from ETH Zurich.

Mathias Zambach received the B.Sc. degree in medicine from the Copenhagen University, Copenhagen, Denmark, in 2015 and the B.Sc. degree in engineering from the Technical University of Denmark, Kongens Lyngby, Denmark, in 2018. He received the M.Sc. degree in physics and nanotechnology from the Technical University of Denmark in 2020. He is currently working toward the Ph.D. degree in magnetism and quantum material with the Magnetism and Quantum Materials Group, Technical University of Denmark.

He has a broad background in physics and nanotechnology and his current research interests include static and dynamic susceptibility of magnetic nanoparticles, losses and heating mechanisms in magnetic nanoparticles, and design of magnetic particles for composite magnetic materials for high-frequency inductor cores.

Cathrine Frandsen is currently a Professor in physics with the Technical University of Denmark, Kongens Lyngby, Denmark. She is author of ca. 100 papers, including three in science and two patent applications. Her research focuses on magnetic materials, specifically she works on controlling the heating of magnetic nanoparticles in high-frequency fields and exploiting this to design new nanostructured magnetic materials for green energy solutions and health technology.

Prof. Frandsen was the recipient of three awards for her work.

Marco Beleggia received the Ph.D. degree in physics from the University of Bologna, Bologna, Italy, in 2001.

From 2002 to 2007, he was a Postdoctoral Researcher and then an Associate Physicist with Brookhaven National Laboratory, USA. In 2008, he was with the University of Leeds, U.K., and then, from 2009 to 2021, he was an Associate Professor with the Technical University of Denmark. He is currently an Associate Professor of Experimental Physics with the University of Modena and Reggio Emilia, Modena, Italy. He has authored more than 100 peer-reviewed papers with more than 3000 citations and an h-index of 28. His research focuses on coherent electron imaging of advanced functional materials, quantum materials, and biomaterials. His activities cover a broad range of topics, including shape anisotropy, demagnetization fields, magnetic interactions, nanoparticle superstructures, methodology, and instrumental developments for electron imaging of magnetic materials.

Dr. Beleggia is an Associate Editor for IEEE MAGNETICS LETTERS.

Anders Michael Jørgensen received the M.Sc. and Ph.D. degrees from the Technical University of Denmark, Kongens Lyngby, Denmark, in 1998 and 2003, respectively.

He was a Postdoctoral with DTU MIC between 2003 and 2006, working on advanced microfabrication and multidomain integration. From 2006 to 2009, he worked in two start-up companies within photovoltaics. In 2009 he joined the core facility, DTU Nanolab (named DTU Danchip at the time) as the Head of Customer Support and in 2014 he was promoted to the Deputy Director, a title he currently holds. He is the author of more than 30 papers and has contributed to the book Microsystem Engineering of Lab-on-a-Chip Devices (VCH-Wiley, Weinheim, 2003). He holds three international patents. His current research interests are within advanced micro and nanofabrication and characterization. His work focuses on establishing new research facilities with specialty cleanrooms and unique tool sets as part of DTU Nanolab.

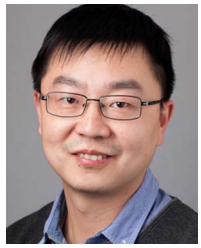

Ziwei Ouyang (Senior Member, IEEE) received the Ph.D degree in power electronics from Technical University of Denmark (DTU), Kongens Lyngby, Denmark, in 2011.

Since from April 2016, he has been an Associate Professor with DTU. He has been appointed as the Head of study in MSc Electrical Engineering since 2021. His research areas focus on switch mode power supply, magnetics modeling and integration, energy storage system, and wireless charging etc. He has more than 110 high impact IEEE journal and conference publications, and 9 international patents.

Dr. Ouyang received the 2021 IEEE TRANSACTIONS ON POWER ELECTRONICS First Place Prize Paper Award, and several best paper awards in IEEE sponsored international conferences.